

# The Galactic plane at faint X-ray fluxes – II. Stacked X-ray spectra of a sample of serendipitous *XMM–Newton* sources

R. S. Warwick,<sup>1</sup>★ K. Byckling<sup>1</sup> and D. Pérez-Ramírez<sup>2</sup>

<sup>1</sup>*Department of Physics and Astronomy, University of Leicester, University Road, Leicester LE1 7RH, UK*

<sup>2</sup>*Departamento de Física, Universidad de Jaén, Campus Las Lagunillas, E-23071 Jaén, Spain*

Accepted 2013 December 11. Received 2013 December 9; in original form 2013 October 28

## ABSTRACT

We have investigated the X-ray spectral properties of a sample of 138 X-ray sources detected serendipitously in *XMM–Newton* observations of the Galactic plane, at an intermediate to faint flux level. We divide our sample into five subgroups according to the spectral hardness of the sources, and stack (i.e. co-add) the individual source spectra within each subgroup. As expected these stacked spectra show a softening trend from the hardest to the softest subgroups, which is reflected in the inferred line-of-sight column density. The spectra of the three hardest subgroups are characterized by a hard continuum plus superimposed Fe-line emission in the 6–7 keV bandpass. The average equivalent width (EW) of the 6.7-keV He-like Fe  $K\alpha$  line is  $170^{+35}_{-32}$  eV, whereas the 6.4-keV Fe K fluorescence line from neutral iron and the 6.9-keV H-like Fe  $Ly\alpha$  line have EWs of  $89^{+26}_{-25}$  and  $81^{+30}_{-29}$  eV, respectively, i.e. roughly half that of the 6.7-keV line. The remaining subgroups exhibit soft thermal spectra. Virtually all of the spectrally soft X-ray sources can be associated with relatively nearby coronally active late-type stars, which are evident as bright near-infrared (NIR) objects within the X-ray error circles. On a similar basis only a minority of the spectrally hard X-ray sources have likely NIR identifications. The average continuum and Fe-line properties of the spectrally hard sources are consistent with those of magnetic cataclysmic variables but the direct identification of large numbers of such systems in Galactic X-ray surveys, probing intermediate to faint flux levels, remains challenging.

**Key words:** stars: dwarf novae – novae, cataclysmic variables – X-rays: binaries – X-rays: stars.

## 1 INTRODUCTION

From the ground breaking discoveries of missions, such as *Uhuru*, *SAS-3*, *Ariel V* and *HEAO-1*, that date back over three decades, right through to the present era of observatory class missions, such as *Chandra*, *XMM–Newton* and *Suzaku*, the study of X-ray bright Galactic sources has been a key theme within high-energy astrophysics. As a result we now have extensive knowledge of the most luminous X-ray emitters in our Galaxy (with X-ray luminosity typically in the range  $10^{35-38}$  erg s<sup>-1</sup>), which in the main can be divided into either low-mass or high-mass X-ray binaries (LMXBs or HMXBs) powered by the accretion of matter on to either a neutron star or black hole (e.g. Grimm, Gilfanov & Sunyaev 2002; Ebisawa et al. 2003). At intermediate X-ray luminosities (nominally  $10^{32-35}$  erg s<sup>-1</sup>) other types of source in addition to X-ray binaries enter the mix, including bright supernova remnants, cata-

clysmic variables (CVs) powered by accretion on to a white dwarf star, massive stars with shock-heated winds and the most extreme coronally active binaries, such as RS CVn systems (e.g. Hertz & Grindlay 1984; Motch et al. 2010). Finally, at relative low X-ray luminosities ( $L_X < 10^{32}$  erg s<sup>-1</sup>) the local population of coronally active stars and binaries dominate the source statistics, particularly in the soft X-ray regime (e.g. Güdel 2004).

Despite the great advances in our understanding of the various classes of Galactic X-ray source, our knowledge of the population properties, such as the number density, the exact form of the luminosity function and the Galactic distribution, remains very incomplete. This is of particular relevance for modern day Galactic surveys conducted in the hard X-ray band (i.e. above 2 keV) where, for sources of intermediate luminosity, the visible volume can extend beyond the Galactic Centre to encompass the bulk of the Galactic disc. Ideally one would use such surveys to construct large samples of identified sources from which the properties of the various populations might be inferred. In practice the identification of the counterparts to hard X-ray sources in the Galactic plane,

★ E-mail: [rsw@star.le.ac.uk](mailto:rsw@star.le.ac.uk)

even with subarcsec X-ray positions, is extraordinarily difficult due to the crowded nature of the star fields and the effects of extinction at optical and near-infrared (NIR) wavelengths (e.g. Ebisawa et al. 2005; Laycock et al. 2005; van den Berg, Hong & Grindlay 2009). Even when likely counterparts are identified, their follow-up, including distance determination, can often present significant challenges (e.g. Motch et al. 2010; van den Berg et al. 2012; Nebot Gómez-Morán et al. 2013).

One way of constraining the properties of low to intermediate luminosity source populations is through their integrated emission. In the Galactic context, the spectrally hard Galactic Ridge X-ray Emission (GRXE; Worrall et al. 1982; Warwick et al. 1985; Koyama et al. 1986a; Yamauchi et al. 1996) has been interpreted both in terms of the superposition of faint point sources (Sugizaki et al. 2001; Revnivtsev et al. 2006; Yuasa, Makishima & Nakazawa 2012) and as a highly energetic, very high temperature phase of the interstellar medium (Koyama, Ikeuchi & Tomisaka 1986b; Kaneda et al. 1997; Tanaka 2002), amongst other possibilities (e.g. Valinia et al. 2000). The GRXE is seen as a narrow ridge of emission extending out to  $|l| \sim 60^\circ$ , but with a surface brightness that peaks towards the Galactic Centre (Yamauchi & Koyama 1993; Revnivtsev et al. 2006; Koyama et al. 2007). In the 4–10 keV band the spectrum of the GRXE matches that of 5–10 keV optically thin CIE thermal plasma with prominent Fe lines at 6.67 and 6.97 keV arising from K-shell emission in He-like and H-like ions (Koyama et al. 1986a; Kaneda et al. 1997). An Fe  $K\alpha$  line at 6.4 keV resulting from the fluorescence of neutral or near-neutral iron is also evident in the X-ray spectrum of the GRXE (Koyama et al. 1996; Ebisawa et al. 2008; Yamauchi et al. 2009). Hereafter we refer to the three prominent Fe  $K\alpha$  lines as the 6.4-, 6.7- and 6.9-keV lines. Below 4 keV, emission lines of abundant elements such as Mg, Si, S, Ar and Ca are also evident in the spectrum of the GRXE, with the intensity ratios of the K lines associated with the He-like and H-like ions of each element (including those of Fe) indicative of a multitemperature plasma (Kaneda et al. 1997; Tanaka 2002). The temperature structure appears to be similar at different locations along the GRXE, with the exception of the region within a degree or so of the Galactic Centre (Uchiyama et al. 2011, 2013).

It has also been reported that above 10 keV the GRXE spectrum exhibits a hard power-law tail, which extends to the hard X-ray/ $\gamma$ -ray region (Yamasaki et al. 1997; Valinia & Marshall 1998; Strong et al. 2005; Krivonos et al. 2007).

Recent studies have shown that the GRXE surface brightness follows that of the NIR light associated with the old stellar population of the Galaxy (Revnivtsev et al. 2006). Also very deep *Chandra* observations have directly resolved over 80 per cent of the GRXE near the Galactic Centre into point sources (Revnivtsev et al. 2009). Taken together this is compelling evidence for the origin of the bulk of GRXE in the integrated emission of point sources, although there is still some debate as to whether there might remain some excess emission attributable to a distinct very hot diffuse component within  $2^\circ$  of the Galactic Centre (Uchiyama et al. 2011, 2013; Heard & Warwick 2013; Nishiyama et al. 2013).

The next key step is to identify the Galactic source population or populations that give rise to the GRXE. The first requirement, in this regard, is that the source population should have a sufficiently high volume emissivity (essentially the product of the mean space density and mean X-ray luminosity) to explain the observed surface brightness of the GRXE. A second constraint is that the integrated spectrum of the sources should match the observed spectrum of the GRXE. In this context it has been proposed that a mix of magnetic CVs plus coronally active binaries may have sufficient

spatial density and hard X-ray luminosity to account for the bulk of the GRXE and its extension into the Galactic Centre (Muno et al. 2004; Revnivtsev et al. 2006, 2008; Sazonov et al. 2006). Also CVs and active binaries have marked spectral similarities to the GRXE (Revnivtsev et al. 2006; Tanaka & Yamauchi 2010; Yuasa et al. 2012). However, as noted earlier, the current uncertainties relating to the population properties and statistics leave many of the details of this model to be confirmed.

In Warwick, Pérez-Ramírez & Byckling (2011, hereafter Paper I), we investigated the serendipitous X-ray source population in the Galactic plane, utilizing the Second *XMM-Newton* Serendipitous Source Catalogue (2XMMi; Watson et al. 2009). The current paper (Paper II) builds on the work in Paper I by focusing on the X-ray spectral properties of a subset of sources with relatively good photon statistics. In Paper I, we showed that the great majority (i.e. >90 per cent) of the spectrally soft X-ray sources may be identified with relatively local coronally active stars; however, the nature of the spectrally hard X-ray sources remains unclear. The goal of the current paper is therefore to investigate the X-ray spectral properties of a sample of sources representative of the source population present in the Galactic plane at intermediate to faint X-ray fluxes. A key question is whether a reasonable number of such sources have the characteristics of CVs, consistent with the hypothesis that CVs contribute significantly to the GRXE.

The remaining sections of this paper are organized as follows. In the next section we discuss how we defined our source sample and extracted X-ray spectral data for each source from the *XMM-Newton* science data archive. To carry out meaningful spectral analysis, we have divided our sample of sources into five subgroups based on the source spectral hardness and stacked (i.e. co-added) the individual source spectra within each subgroup (Section 3). In Section 4, we analyse and compare the stacked spectra for the different subgroups. We go on to investigate the incidence of longer wavelength counterparts by cross-correlating our X-ray source positions with NIR catalogues (Section 5). In Section 6 we discuss our results in the context of the likely contribution of magnetic CVs to the GRXE. Finally, we briefly summarize our main conclusions.

## 2 THE SOURCE SAMPLE AND DATA REDUCTION

In Paper I we discuss the selection and properties of a sample of 2204 serendipitous X-ray sources drawn from 116 *XMM-Newton* observations with pointings in the Galactic plane towards the central quadrant of the Galaxy. Here we focus on a subset of sources from this original sample with a view to extending the spectral analysis beyond the hardness ratio (HR) and ‘band index’ considerations of Paper I.

The selection of objects for this new study was based on the following requirements: (i) the source was detected in the European Photon Imaging Camera (EPIC) pn camera in an observation in which the medium filter was deployed; (ii) there were a nominal 200–1200 pn counts associated with the source (more specifically the product of the 0.5–12 keV pn count rate times the effective source exposure time was in the quoted range); (iii) if there were multiple observations of the same source, the observation with the longest exposure time and/or better quality data was selected. After applying these criteria, the sample reduced to 138 sources drawn from 63 different *XMM-Newton* observations (hereafter we refer to this set of 138 sources as the *current* sample).

Brief details of the sources comprising the current sample are given in Appendix A. The distribution in Galactic longitude and

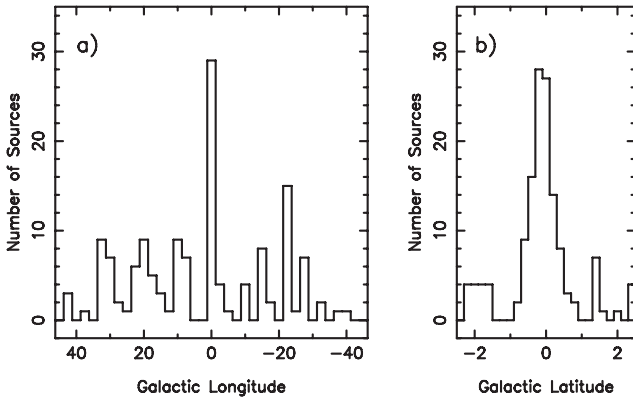


**Figure 1.** (a) The distribution in Galactic longitude of the sources comprising the current sample. (b) The same in Galactic latitude.

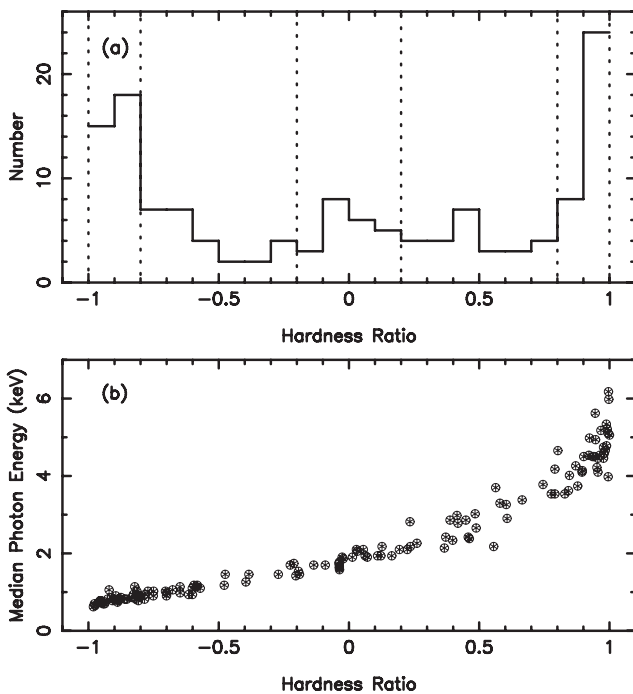


**Figure 2.** (a) The distribution of the broad-band (0.5–2:2–12 keV) HR within the current sample. The vertical dotted lines define the ranges used to select the five source subgroups (see Table 1). (b) The median photon energy (keV) in the source spectrum plotted versus the broad-band HR for each source.

latitude is shown in Fig. 1. The bulk of the sources are located within  $\pm 1^\circ$  of the Galactic plane and roughly 20 per cent lie within  $\approx 1^\circ$  of the Galactic Centre.

In Paper I we categorized sources as spectrally hard or soft depending on whether their broad-band HR,<sup>1</sup> was positive or negative. In keeping with the parent sample, the current sample splits fairly evenly into the soft and hard source categories as illustrated in Fig. 2(a). An alternative approach to the use of HRs to classify the spectral properties of X-ray sources with limited count statistics is to employ ‘quantile’ analysis (e.g. Hong, Schegel & Grindlay 2004)

<sup>1</sup> More specifically,  $HR = (H - S)/(H + S)$ , where  $H$  corresponds to the 2XMMi Bands 4 and 5 (2–12 keV) and  $S$  to Bands 2 and 3 (0.5–2 keV) – see Paper I for details.

and, in that context, Fig. 2(b) compares the *median* photon energy in the (background-subtracted) source spectrum,  $E_{50}$ , with the corresponding value of HR for each source. For the current sample,  $E_{50}$  ranges from 0.5 keV at the soft extreme up to a maximum of  $\approx 6$  keV for the hardest sources.

Given that the source selection is based on a total count criterion, there is a wide spread in the count rates of the selected objects. For the great majority of the sources the count rate is in the range 5–100 pn count  $\text{ks}^{-1}$  in either or both of the soft and hard bands (cf. fig. 5 in Paper I). For the soft sources, the flux range sampled is  $0.1\text{--}2 \times 10^{-13}$   $\text{erg cm}^{-2} \text{s}^{-1}$  (0.5–2 keV) and for the hard sources,  $0.6\text{--}12 \times 10^{-13}$   $\text{erg cm}^{-2} \text{s}^{-1}$  (2–10 keV).

The present analysis is based on spectral data solely from the EPIC pn camera. We extracted the pn spectrum of each source using the *XMM-Newton* Science Analysis System (SAS) and standard techniques. In brief, each data set was reprocessed in order to apply the most recent calibration and screened for high background flares by applying a cut when the full-field count rate in the 10–12 keV band exceeded  $0.4 \text{ count s}^{-1}$ . Only single or double X-ray events were chosen with `PATTERN = 0–4` and with `FLAG = 0` (the latter excluding events close to chip gaps, bad pixels or inoperative columns). The source spectra were extracted within a circular region of radius  $r = 35$  arcsec ( $= 700$  pixels) for most of the sources. However, for 13 sources the radius of the source extraction region was calculated using the SAS task `REGION` in order to minimize possible contamination from nearby sources. The background was taken from a circular extraction region with a radius of  $r = 120$  arcsec ( $= 2600$  pixels); in general, the background region was positioned on the same CCD chip as the source (or occasionally on an adjacent chip). Finally, the redistribution matrix files (RMFs) and the ancillary response files (ARFs) were created using `RMFGEN` and `ARFGEN` for each individual source spectrum.

### 3 STACKING OF THE SOURCE SPECTRA

After background subtraction, the net number of counts actually recorded for each source was typically in the range 100–800 (see Table A1). The measured counts were generally reduced compared to the prediction used in source selection due to two effects; the loss of signal lying in the wings of the point spread function (PSF) outside of the source extraction circle and the use of a more stringent threshold for the data filtering than employed in the production of the 2XMMi catalogue.

Since individually the sources have insufficient counts for detailed spectral analysis (although see Section 4.2), the full sample of 138 sources was divided into five subgroups (H, MH, MD, MS and S) based on the source spectral hardness (see Fig. 2 and Table 1). Within each of these five subgroups the source spectra

**Table 1.** The designation and HR range for the five source subgroups. The number of sources contributing and the total counts per subgroup, net of the background, are also quoted.

Subgroup	Hardness ratio	Number of sources	Total net counts
H	1.0–0.8	32	8221
MH	0.8–0.2	25	6729
MD	0.2–(–0.2)	22	7667
MS	–0.2–(–0.8)	26	6906
S	–0.8–(–1.0)	33	11 449

were stacked. After applying a scaling so as to match the area of the background region to that of the source extraction region, the associated background spectra were similarly co-added. The RMF and ARF files of each individual source spectrum were combined by using the `FTOOL MARFRMF v.2.2.0`. Thereafter, the individual output files from `MARFRMF` were combined in `ADDRMF v.1.21` so as to give a total response file applicable to the stacked spectra for each source subgroup. Finally, the spectra were binned using the `FTOOL GRPPHA`; eight-channel binning (of the 4096 input PHA channels) was employed in the case of the spectra pertaining to the H, MH and MD subgroups, whereas for the MS and S subgroups, four- and eight-channel binning was applied to the PHA ranges 0–511 and 512–4095, respectively.

Source statistics for the five subgroups are given in Table 1. Summed over the full set of 138 sources, 40 972 pn counts were recorded in the 0.5–12 keV band, net of the background.

The spectra of the five subgroups after background subtraction are illustrated in Fig. 3, together with the composite spectrum for the full sample. A very clear spectral softening trend is evident from the H through to the S subgroups (rather as expected). The spectra of subgroups H and MH show strong soft X-ray absorption and also evidence for Fe features in the 6–7 keV band. The MD subgroup

spectrum retains a hard tail out to  $\sim 7$  keV, which is barely present in the spectrum of MS subgroup and completely absent from that of the S subgroup.

## 4 X-RAY SPECTRAL ANALYSIS

The analysis of the five stacked spectra was carried out using `XSPEC` version 12.8.1 (Arnaud 1996). The spectral fits were limited to the energy range 2–9 keV for the H subgroup and to 1–9 keV for both the MH and MD subgroups. In each case, data between 7.8 and 8.3 keV were excluded in order to eliminate the effect of background subtraction residuals pertaining to the  $K\alpha$  Cu fluorescence lines in the detector background. For the MS and S subgroups, we used the energy range 0.5–5 keV.

### 4.1 The spectral models

The X-ray spectra of the H, MH and MD subgroups were investigated using a spectral model comprising a power-law continuum plus three Gaussian emission lines at fixed energies of 6.41, 6.68 and 6.96 keV. As noted earlier, these three lines correspond to  $K\alpha$  emission from neutral (or near-neutral) Fe atoms, He-like Fe ions

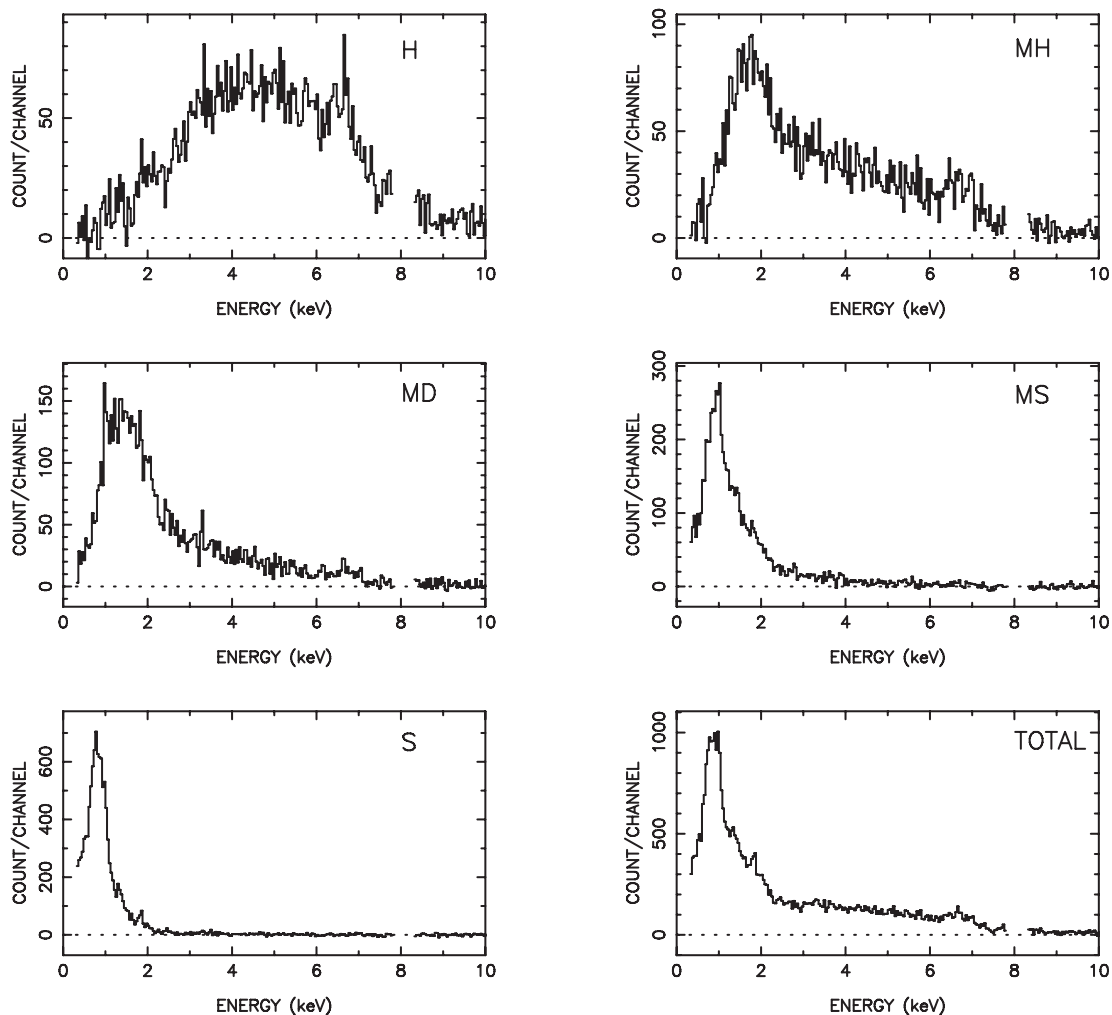


**Figure 3.** The background-subtracted spectra for the five source subgroups H, MH, MD, MS and S, together with the composite spectrum for all 138 sources (lower right-hand corner). The data between 7.8 and 8.3 keV (i.e. the region of the  $K\alpha$  Cu fluorescence lines in the detector) have been excluded. The horizontal dotted line indicates the level of zero net counts per channel.

**Table 2.** Top section: the best-fitting parameters from the spectral fitting of an absorbed power law plus emission lines model to the spectra of the H, MH and MD subgroups. The columns give the derived column density,  $N_{\text{H}}$ , the photon index,  $\Gamma$ , the equivalent width, EW, of the three Fe lines and the reduced  $\chi^2_{\nu}$  and number of degrees of freedom  $\nu$  for the fit. Lower section: the best-fitting parameters from the spectral fits to the spectra of the S, MS and MD subgroups, incorporating various combinations of thermal plasma and power-law components. The columns list  $N_{\text{H}}$ ,  $\Gamma$ , two plasma temperatures  $kT_{\text{cool}}$  and  $kT_{\text{hot}}$ , the derived metal abundance  $Z_{\odot}$  relative to solar. The reduced  $\chi^2_{\nu}$  and the number of degrees of freedom  $\nu$  for the fit are also quoted.

Group	$N_{\text{H}}$ ( $\times 10^{22} \text{ cm}^{-2}$ )	$\Gamma$	EW (6.4 keV) (eV)	EW (6.7 keV) (eV)	EW (6.9 keV) (eV)	$\chi^2_{\nu}/\nu$
H	$8.3^{+0.6}_{-0.5}$	$1.55^{+0.07}_{-0.07}$	$94^{+30}_{-30}$	$149^{+35}_{-34}$	$55^{+34}_{-33}$	1.16/517
MH	$1.27^{+0.12}_{-0.10}$	–	$152^{+53}_{-53}$	$172^{+51}_{-51}$	$192^{+65}_{-65}$	–
MD	$0.34^{+0.07}_{-0.06}$	–	<88	$187^{+89}_{-91}$	$56^{+73}_{-56}$	–
Joint EW	–	$1.54^{+0.07}_{-0.07}$	$89^{+26}_{-25}$	$170^{+35}_{-32}$	$81^{+30}_{-29}$	1.20/523
	$N_{\text{H}}$ ( $\times 10^{22} \text{ cm}^{-2}$ )	$\Gamma$	$kT_{\text{cool}}$ (keV)	$kT_{\text{hot}}$ (keV)	$Z_{\odot}$	$\chi^2_{\nu}/\nu$
S	$0.057^{+0.034}_{-0.022}$	–	$0.51^{+0.13}_{-0.12}$	$1.01^{+0.14}_{-0.06}$	$0.13^{+0.02}_{-0.02}$	1.17/159
MS	$0.18^{+0.02}_{-0.02}$	–	1.0 (fixed)	$3.6^{+1.1}_{-0.7}$	0.13 (fixed)	0.85/160
MD	$0.87^{+0.05}_{-0.05}$	1.55 (fixed)	1.0 (fixed)	–	0.13 (fixed)	1.05/96

and H-like Fe ions, respectively. The intrinsic widths of the three lines were fixed at  $\sigma = 30$  eV (e.g. Koyama et al. 2007; Capelli et al. 2012). The emission components were subject to a line-of-sight absorption column density,  $N_{\text{H}}$ , (using PHABS in XSPEC). A joint fit was employed, initially, with only the power-law photon index,  $\Gamma$ , tied across the three data sets. The results of this analysis are summarized in the first three lines of Table 2, where the line strengths are quoted in terms of their equivalent width (EW) with respect to the underlying continuum. Here the errors are at 90 per cent confidence, except for the upper limit which is quoted at  $3\sigma$ .

From the results in Table 2, it is evident that the simple absorbed power law plus lines model provides a reasonable description of the data. The HR selection criterion used to define the three source samples is reflected in the derived  $N_{\text{H}}$  which varies from  $\approx 8 \times 10^{22} \text{ cm}^{-2}$  for the H subgroup to  $\approx 3 \times 10^{21} \text{ cm}^{-2}$  for the MD subgroup. The derived photon index,  $\Gamma = 1.55 \pm 0.07$ , demonstrates that the sources contributing to the stacked spectra have, on average, rather hard continuum spectra. When the power-law continuum is replaced by a thermal bremsstrahlung continuum, a correspondingly high temperature is derived,  $kT = 19^{+6}_{-4}$  keV, with only marginal changes in the other spectral parameters and the  $\chi^2$  of the fit.

The presence of a 6.7-keV Fe line is a feature common to the H, MH and MD subgroups. There is also evidence for the 6.9-keV line in the H and MH spectra and weakly in the MD spectrum. Similarly the 6.4-keV Fe line is detected in the spectra of the two hardest subgroups, but not in the MD spectrum. Fig. 4 illustrates the form of the measured spectrum and the corresponding best-fitting spectral model in the region of the iron line complex for the H subgroup.

In order to determine the line EWs averaged over the three data sets we repeated the absorbed power law plus Fe lines spectral fitting with the EWs of the three lines tied across the H, MH and MD spectra (in addition to the photon index of the power-law continuum). The result is reported in Table 2 on the line labelled Joint EW. In summary the average EW of the 6.7-keV line measured in the full sample of sources with  $\text{HR} > -0.2$  is  $\approx 170$  eV, with the 6.4- and 6.9-keV lines coming in at approximately half this value.

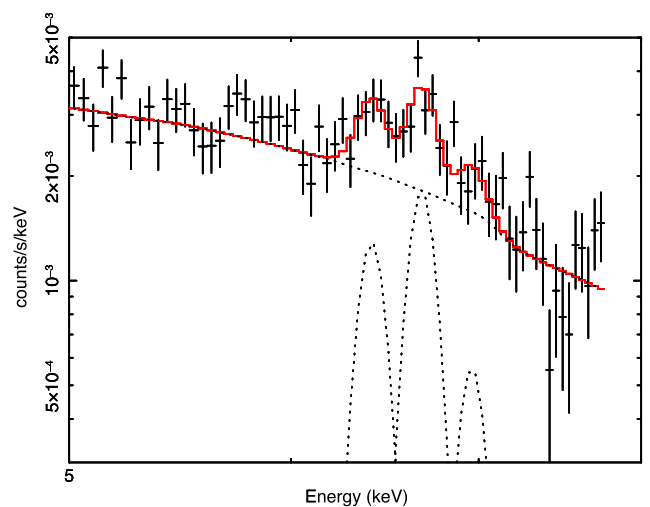


**Figure 4.** The H subgroup spectrum around the iron line complex. The contribution to the best-fitting model of the power-law continuum and each of the Fe line components is shown as black dotted lines with the combined fit shown in red.

A simple absorbed power-law model provided a poor description of the spectra pertaining to the MS and S subgroups. Accordingly these spectra were fitted using a two-temperature thermal plasma model, which is a commonly used approximation for systems exhibiting a broad span of emission measure versus temperature. In XSPEC this was achieved by employing two APEC components with a tied metal abundance  $Z_{\odot}$ . The latter parameter was, nevertheless, allowed to vary (as a single scale factor applied to the standard solar abundance ratios defined by Anders & Grevesse 1989). The same foreground column density was assumed to apply to both thermal components.

The fitting of the spectrum of the softest subgroup resulted in temperatures close to 0.5 and 1.0 keV for the cooler and hotter components, respectively – as reported in the lower section of

Table 2. In this model the 1-keV component contributes 68 per cent of the observed 0.5–2 keV flux. The inferred metal abundance within thermal plasma is extremely subsolar, but this is most probably an artefact of the two-temperature spectral approximation, as has been noted by many authors (e.g. Strickland et al. 2000). The combination of the low derived  $N_{\text{H}}$  and a two-temperature description of the emission spectrum is fully consistent with the underlying source population being nearby, coronally active stars.

We next attempted to use the same emission model ( $kT$  values fixed at 0.5 and 1 keV and  $Z_{\odot}$  set to 0.13) to fit the spectrum of the MS data set but failed to obtain a satisfactory result. In fact, the presence of a (modest) hard tail within this data set requires a hotter thermal component, with the additional  $N_{\text{H}}$  likely masking the soft emission characterized by the 0.5-keV component. The best fit obtained when the temperature of the latter component was allowed to vary is reported in Table 2. In this case the 1-keV emission is the cooler component with the hotter  $\sim 3$  keV emission contributing 51 per cent of the observed 0.5–2 keV flux. The inferred column density for the MS subgroup is approximately three times that of the S subgroup. If we (naively) interpret this in terms of the MS sources being typically at three times the distance of those in the S subgroup, then the implication is that the former are on average an order of magnitude more X-ray luminous (since the same flux threshold applies in the two cases). The hotter emission of the MS subgroup might therefore reflect higher levels of coronal activity and the probable inclusion of some active binaries.

Given that coronally active stars and binaries likely dominate the MS and S subgroups, but certainly not the MH and H subgroups (see Paper I and Section 5), it is safe to assume that the MD subgroup includes both soft and hard population objects. When we reconsider the spectral fitting of the MD subgroup (in this case in the restricted 1–5 keV band), we find that the inclusion of a 1-keV thermal plasma component (along with the  $\Gamma = 1.55$  power law) gives a significant improvement to the fit (as measured by  $F_{\text{TEST}}$  routine in *XSPEC*). The best-fitting parameters for this power law plus thermal model are provided as the last entry in Table 2. In this model, the thermal component contributes roughly 20 per cent of the 1–5 keV flux. Thus the MD subgroup does seem to comprise a mix of source populations. We note, however, that the presence of a number of sources with intrinsically soft spectra in the MD subgroup is unlikely to have an undue impact on the Fe line EW measurements, since such sources will contribute little to either the lines or the underlying continuum in the 6–7 keV band.

#### 4.2 Fe-line properties of the individual sources

In order to investigate the contribution of individual sources to the Fe-line emission in the H, MH and MD subgroups, we extracted the counts recorded for each source in a narrow bandpass (of width 240 eV) centred on each Fe line. The level of the underlying continuum appropriate to each measurement was also estimated based on a linear interpolation of the counts recorded in two ‘continuum’ bands (each of width 600 eV) centred at 5.94 and 7.54 keV. Fig. 5 shows a plot of the net line counts in the 6.4-, 6.7- and 6.9-keV lines versus the HR for the full set of sources that comprise the three subgroups. In this figure the data points plotted in red correspond to those sources for which the line measurement represents a ‘detection’ at or above the  $2.5\sigma$  significance level. The number of sources with directly detectable lines at 6.4, 6.7 and 6.9 keV is 2, 6 and 1, respectively, with just one source exhibiting more than a single line (158770 – with twin features at 6.7 and 6.9 keV). A summary of the Fe-line properties of these eight sources is provided in Table 3.

In broad terms, Fig. 5 confirms the results of the spectral fitting of the source subgroups. In the case of the 6.7-keV line, there is a positive bias in the EW measurements, particularly for the sources within the H and MH categories ( $\text{HR} > 0.2$ ). The 6.4 and 6.9 keV measurements also fit this description.

There is a suggestion that the relatively high line EWs measured in the MH subgroup (see Table 2) may be due to the influence of two sources – source 168031 which has a relatively bright 6.4-keV line and, as noted above, source 158770 which exhibits detectable line features at both 6.7 and 6.9 keV. Fig. 6 illustrates the X-ray spectra of these two sources in comparison to the spectra of two ‘typical’ sources drawn from the H subgroup, one with a detectable 6.4-keV line and the other with a 6.7-keV feature. If we exclude the two sources identified above from the MH sample, the impact is to reduce the EW values tabulated for the MH subgroup in Table 2 by about 30 per cent; however, such an exclusion would be somewhat arbitrary.

## 5 NIR COUNTERPARTS OF THE SOURCES

We have searched for potential NIR counterparts of the X-ray sources in the current sample by cross-matching the *XMM-Newton* source positions with the Two Micron All Sky Survey (2MASS)<sup>2</sup> (Cutri et al. 2003; Skrutskie et al. 2006). The methodology for the cross-matching was essentially the same as that reported in Paper I, where full details are provided.

We found that of the 59 sources in the S and MS subgroups, 53 (90 per cent) have a bright ( $K_{\text{S}} < 14$ ) 2MASS star within a  $3\sigma$  error radius of the X-ray position (i.e. within an error circle with radius equal to three times the X-ray position error quoted in the 2XMMi ‘slim’ catalogue).<sup>3</sup> There are three further likely 2MASS counterparts if the error circles are extended to  $3.25\sigma$ . The remaining three sources include one instance where the 2MASS catalogue suffers from the confusion of a bright nearby star and, similarly, two instances where the X-ray position may be marginally offset due to the confusion of a nearby X-ray source. In short, virtually all of the soft X-ray sources have plausible NIR-bright counterparts, the majority of which are likely to be nearby, coronally active stars and binaries (see Paper I).

The NIR associations for the harder spectral subgroups are much less complete. For the MD subgroup, 13 sources out of 22 (59 per cent) have bright ( $K_{\text{S}} < 14$ ) 2MASS objects in a nominal  $3\sigma$  X-ray error circle, whereas for the MH and H subgroups the statistics are 10 out of 25 (40 per cent) and 8 out of 32 (25 per cent), respectively. The average (area-weighted)  $3\sigma$  error circle radius for the current sample of sources is 2.5 arcsec. Utilizing a set of positions offset from each X-ray position, we find that, for these Galactic plane fields, the corresponding chance coincidence rate with 2MASS stars brighter than  $K_{\text{S}} = 14$  is 15 per cent. Fig. 7 summarizes these statistics. The implication is that, at least within the MD and MH subgroups, a sizeable minority of sources may have real identifications with bright NIR stars.

We have plotted a NIR two-colour diagram for the 2MASS stars contained within the X-ray error circles in Fig. 8 (but excluding sources with relatively poor photometry for which the 2MASS Q flag = U in one or more bands). In this diagram the bulk of the

<sup>2</sup> <http://www.ipac.caltech.edu/2mass/>

<sup>3</sup> In the case of multiple observations of an X-ray source, the X-ray position and position errors quoted in the 2XMM ‘slim’ catalogue are the weighted average value across *all* the detections of the source.

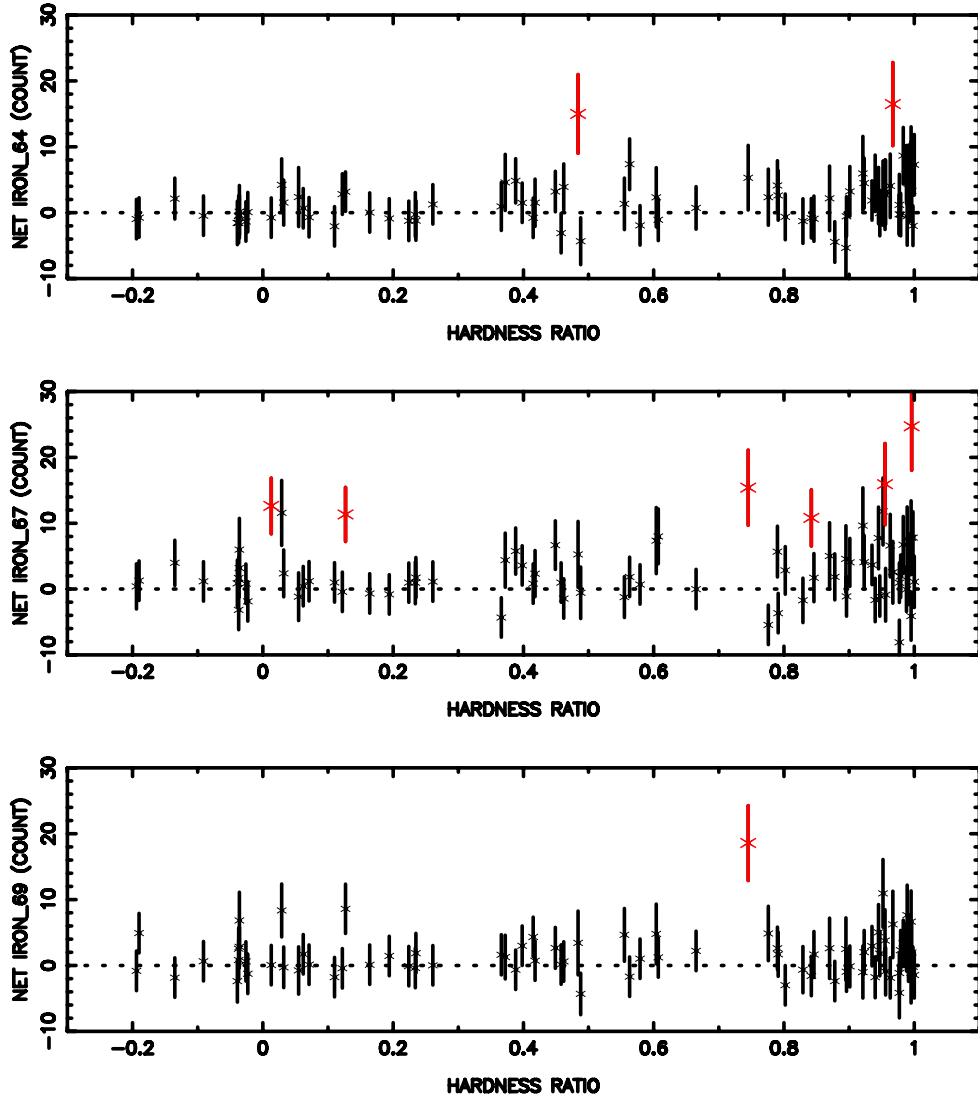


**Figure 5.** The net counts of the 6.4-keV (top panel), 6.7-keV (middle panel) and 6.9-keV (bottom panel) Fe lines versus the HR for each source. The red data points represent the sources with a significant ( $2.5\sigma$ ) number of net counts in the line (see Table 3).

**Table 3.** The eight individual sources in which one or more of the Fe lines (at 6.4, 6.7 and 6.9 keV) was detected above  $2.5\sigma$ . The table lists the net count in the three lines for each source and also quotes the EW if the line was detected above  $2.5\sigma$ .

Source	212279	148374	168031	158770	166494	151081	217813	157004
HR	0.01	0.13	0.48	0.75	0.84	0.95	0.97	1.00
Net counts (6.4 keV)	$-0.8 \pm 3.0$	$3.2 \pm 3.0$	$15.0 \pm 6.0$	$5.3 \pm 4.9$	$-0.8 \pm 3.0$	$2.7 \pm 5.3$	$16.5 \pm 6.3$	$3.3 \pm 4.7$
EW (eV)	–	–	$674 \pm 269$	–	–	–	$244 \pm 93$	–
Net counts (6.7 keV)	$12.6 \pm 4.2$	$11.3 \pm 4.1$	$5.3 \pm 5.0$	$15.4 \pm 5.7$	$10.8 \pm 4.3$	$15.9 \pm 6.2$	$2.6 \pm 4.7$	$24.7 \pm 6.7$
EW (eV)	$1218 \pm 409$	$2945 \pm 1066$	–	$508 \pm 188$	$1210 \pm 477$	$329 \pm 127$	–	$635 \pm 171$
Net counts (6.9 keV)	$0.1 \pm 3.0$	$8.6 \pm 3.7$	$3.4 \pm 4.8$	$18.6 \pm 5.7$	$-1.6 \pm 3.0$	$3.8 \pm 4.7$	$6.2 \pm 5.0$	$2.0 \pm 4.4$
EW (eV)	–	–	–	$686 \pm 210$	–	–	–	–

objects associated with X-ray sources in the S and MS categories fall on the locus of late-type main-sequence stars with relatively low reddening. In contrast, the stars linked to the X-ray sources in the MD through to H subgroups are characterized by an increasing degree of reddening.

We have also plotted a colour–magnitude diagram for the same set of NIR objects in Fig. 9 (as the circular symbols). This figure also

shows the tracks of several different types of stellar objects in the colour–magnitude plane assuming that the visual absorption,  $A_V$ , in the Galactic plane increases at the rate of  $2 \text{ mag kpc}^{-1}$  (equivalent to  $A_J = 0.56 \text{ mag kpc}^{-1}$ ,  $A_K = 0.224 \text{ mag kpc}^{-1}$ ). We use a compilation of NIR magnitudes for CVs (Ak et al. 2007, 2008) to estimate the absolute magnitude and intrinsic colour typical of a CV. Similarly, the NIR properties of the dwarf, giant and supergiant stars are

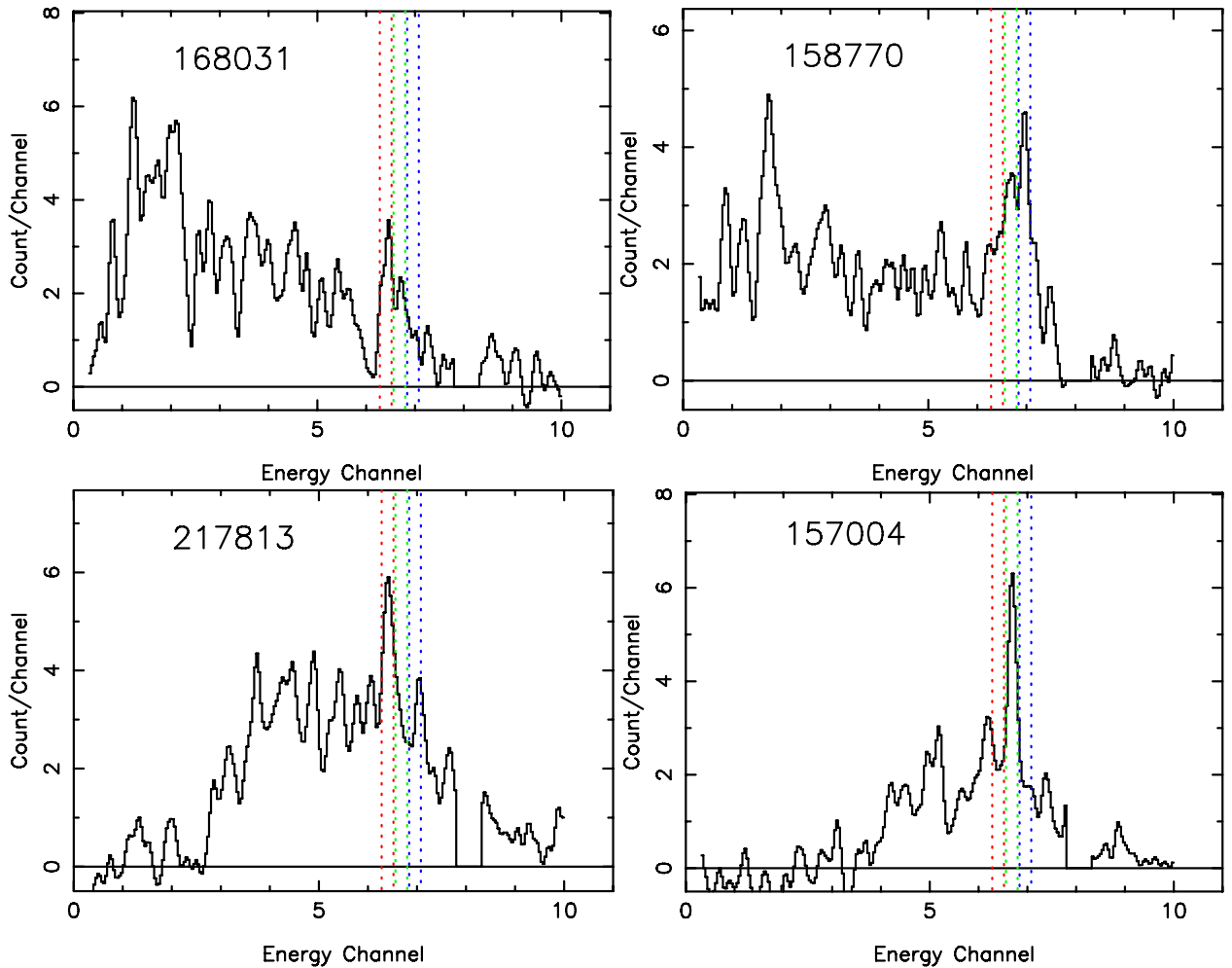


**Figure 6.** The measured source spectrum net of background for four sources. The spectral data have been grouped into 40 eV channels and smoothed with a Gaussian line spread function of width  $\sigma = 60$  eV. The vertical dashed lines indicate the 6.4 (red), 6.7 (green) and 6.9 keV (blue) bandpasses. The data between 7.8 and 8.3 keV (i.e. the region of the  $K\alpha$  Cu fluorescence lines in the detector) have been excluded. Top panels: two sources from the MH subgroup with detectable lines at 6.4 keV (168031) and 6.7 and 6.9 keV (158770). Bottom panels: H subgroup sources with line features at 6.4 (217813) and 6.7 keV (157004).

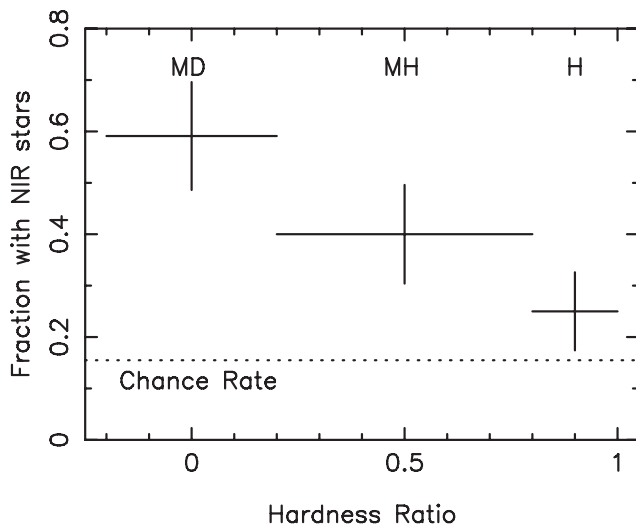


**Figure 7.** The fraction of sources with a bright 2MASS star contained within the X-ray error circle for the MD, MH and H subgroups. The chance rate is indicated by the dotted line.

taken from Covey et al. (2007). This figure illustrates rather clearly that if the association of an X-ray source with a *highly reddened*, but *relatively bright* NIR star (with, say,  $J - K_S > 1.0$  and  $K_S < 14$ ) is real, then it is unlikely that we are dealing with either a distant luminous CV or a very coronally active dwarf (F–M) star. The basic point is that if we interpret a high degree of reddening as indicative of a relatively large distance (i.e. assuming that the reddening is not a feature of the very local environment of the source) then rather faint magnitudes are implied for dwarf stars. It is much more tenable that the association is with either a late-type giant or a bright supergiant (e.g. Mauerhan et al. 2009, 2010; Motch et al. 2010; Nebot Gómez-Morán et al. 2013). The former category includes RS CVn binaries containing a G- or K-type giant twinned with a subgiant or main-sequence companion, which are characterized by enhanced, high-temperature coronal emission driven by tidal interactions (e.g. Agrawal, Riegler & White 1981). If, for example, we observe an RS CVn system containing a K3III giant at  $K_S = 10$ , then the implied distance is  $\approx 2$  kpc. For a limiting flux in the hard band of, say,  $2 \times 10^{-13}$  erg cm $^{-2}$  s $^{-1}$  (2–10 keV), the implied X-ray luminosity,  $L_X$ , is  $\approx 10^{32}$  erg s $^{-1}$ , which is plausible for the most active systems. If the counterpart to the X-ray source is a massive early-type star

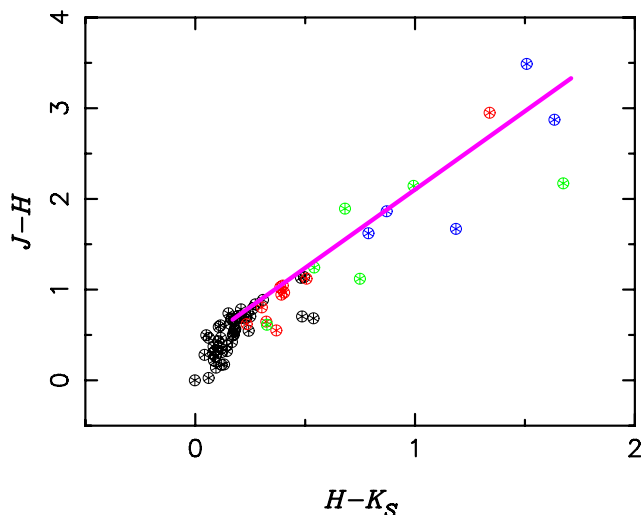


**Figure 8.** The  $H - K_S$  versus  $J - H$  colour–colour diagram of the brightest 2MASS star contained within the X-ray error circle. X-ray sources in the S and MS subgroups are shown as the black symbols, whereas those in the MD, MH and H subgroups are plotted in red, green and blue, respectively. The solid diagonal line illustrates the reddening vector corresponding to  $A_V = 25$  ( $A_J = 7.0$ ,  $A_H = 4.3$ ,  $A_K = 2.8$ ) from a starting point representative of the NIR colours of an unreddened MOV star.

such as a Wolf–Rayet star or an OB supergiant, then a significant X-ray flux above 2 keV may be produced in shocked regions within an unstable wind or, in the case of massive binaries, in the colliding winds. As is evident from Fig. 9, in this case a  $K_S$  magnitude of 10 or fainter implies a hard-band X-ray luminosity considerably greater than  $10^{32}$  erg s $^{-1}$ , which points to either a binary (or multiple) massive star system or the presence of an accreting high-mass X-ray binary (Mauerhan et al. 2010; Anderson et al. 2011; Paper I and references therein).

Fig. 9 also shows a cluster of points representative of the colours and magnitudes of known CVs, when translated to a common distance of 2 kpc, based on the compilation of CV NIR magnitudes and distances reported by Ak et al. (2007, 2008). As noted above for a distance of 2 kpc, our hard-band limiting flux corresponds to an X-ray luminosity of  $\approx 10^{32}$  erg s $^{-1}$ . Clearly, in order to identify such a population of sources amongst our sample of hard X-ray sources, one would need to go to significantly fainter NIR magnitudes than are probed by 2MASS. Typically such counterparts would have  $K_S > 15$ , but be subject to only a modest degree of interstellar reddening. The problem, of course, is that in the Galactic plane at these faint infrared magnitudes, the chance incidence rate of stars may become excessive, at least when using the typical few arcsec error circles available from *XMM–Newton*.

By way of an experiment, we have selected a subset of the hard X-ray sources (within the MD, MH and H subgroups) which have relatively small X-ray error circles ( $3\sigma$  error circle radius  $\leq 1.5$  arcsec) and for which deep NIR imaging is available from the United Kingdom Deep Sky Survey (UKIDSS)<sup>4</sup> (Lawrence et al. 2007). Of the 18 X-ray sources meeting this criterion, we have found possible NIR associations in nine cases. These are shown as the diamond symbols in Fig. 9. Two of these NIR objects (both linked to H subgroup sources) are located in the region of the diagram where we might expect to find X-ray luminous CVs. Interestingly a search of

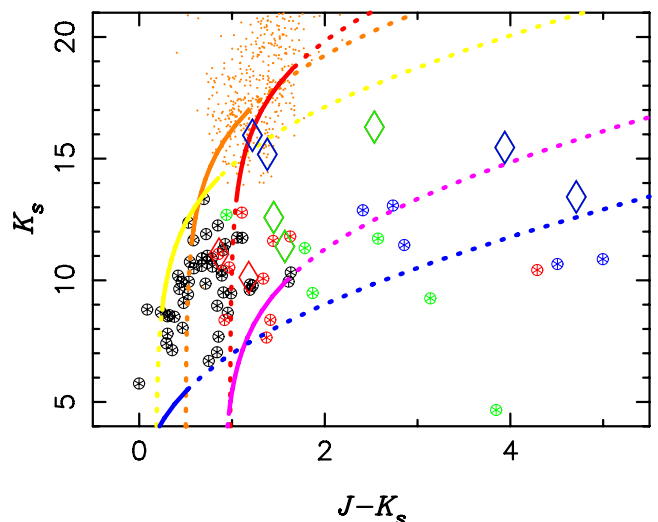


**Figure 9.** The  $J - K_S$  versus  $K_S$  colour–magnitude diagram of the brightest NIR stars contained within the X-ray error circle. The results from the comparison with 2MASS are shown as the circular symbols with colour coding indicative of the X-ray subgroup as follows – S and MS (black), MD (red), MH (green) or H (blue). The diamond symbols show the same information when the study is extended to UKIDSS for a subset of the sources – see the text. The cluster of brown points represents known CVs when their colours and magnitudes are translated to a standard distance of 2 kpc. The curves illustrate the tracks of different types of star as the distance is varied from 1 pc to 20 kpc, assuming that  $A_V$  in the Galactic plane increases at the rate of 2 mag kpc $^{-1}$ . The curves become solid lines for stellar distances in the range 200 pc–2 kpc, which corresponds to an X-ray luminosity in the range  $10^{30-32}$  erg s $^{-1}$ , assuming a limiting X-ray flux of  $2 \times 10^{-13}$  erg cm $^{-2}$  s $^{-1}$  (2–10 keV). Brown curve: a luminous CV with  $M_K = 5.0$  and intrinsic  $J - K_S = 0.5$ ; yellow curve: a FOV dwarf star with  $M_K = 2.25$ ,  $J - K_S = 0.18$ ; red curve: a M6V dwarf with  $M_K = 6.74$ ,  $J - K_S = 0.98$ ; purple curve: a K3III giant with  $M_K = -2.03$ ,  $J - K_S = 0.90$ ; blue curve: a BOI supergiant with  $M_K = -6.44$ ,  $J - K_S = -0.15$ .

the catalogues held at Vizier<sup>5</sup> shows that one of these objects is a known intermediate polar (also known as SAX J1748.2–2808; Ritter & Kolb 2003; Sidoli et al. 2006; Nobukawa et al. 2009). A Vizier search on the full sample of hard X-ray sources also revealed a handful of other likely identifications, including several high reddened sources near the Galactic Centre previously studied by Mauerhan et al. (2009), two LMXB (Liu, van Paradijs & van den Heuvel 2007), a Be star HMXB (Ebisawa et al. 2003) and a potential AM HER object (Motch et al. 2010).

In summary, our cross-correlation with NIR catalogues demonstrates that virtually all the soft X-ray sources in our sample (comprising the S and MS subgroups) can be associated with a bright late-type stellar counterpart possessing an active stellar corona. The nature of the Galactic population or populations underlying the hard X-ray sources (comprising subgroups H, MH and MD) is less clear-cut, although highly coronally active systems such as RSCVn binaries, wind-dominated objects such as Wolf–Rayet stars and OB supergiants and accretion-powered systems ranging from CVs, through to LMXB and HMXBs, all contribute to the mix. Extragalactic interlopers, predominantly active galactic nuclei (AGN) seen through the high column density of the Galactic plane may also represent a significant (maybe 50 per cent) fraction of the

<sup>4</sup> <http://www.ukidss.org/>

<sup>5</sup> <http://vizier.u-strabg.fr/viz-bin/Vizier/>

hardest subgroup of sources (Hands et al. 2004; Paper I). However, our analysis does provide a hint that an appropriate combination of subarcsec X-ray positions and deep high-resolution NIR imaging has the potential to reveal an increasing number of CV counterparts, at least in surveys reaching intermediate rather than very deep X-ray flux thresholds.

## 6 DISCUSSION

Currently, the leading candidate for the unresolved source population contributing to the GRXE is *magnetic* CVs, nearby examples of which typically have 2–10 keV X-ray luminosities in the range from  $10^{31}$  to  $10^{34}$  erg s<sup>-1</sup> (e.g. Ezuka & Ishida 1999; Sazonov et al. 2006; Revnivtsev et al. 2008). In principle this includes both polars (where the spin and orbit are synchronized or nearly synchronized) and intermediate polars (IPs; where the orbital period is much longer than the white dwarf spin period). However, the plasma temperatures of polars are somewhat lower than in IPs due to enhanced cyclotron cooling (e.g. Cropper, Ramsay & Wu 1998) and it is likely that IPs contribute most to the hard X-ray (>5 keV) volume emissivity.

In magnetic CVs, an accretion shock is generated above the white dwarf surface, which heats the accreting material to temperatures  $kT > 15$  keV. The resulting highly ionized, optically thin plasma cools in the post-shock flow and, eventually, settles on to the white dwarf surface through an accretion column. The resulting X-ray spectrum comprises a complex blend of contributions generated at differing temperatures, densities and optical depths (e.g. Cropper et al. 1999; Yuasa et al. 2010). As well as a hard continuum, the X-ray spectra of magnetic CVs are characterized by a complex of Fe K lines including strong He-like, H-like and fluorescent components, the latter arising from the illumination of the surface of the white dwarf and/or the outer regions of the accreting flow by the hard continuum.

In a study of 20 magnetic CVs observed by *ASCA*, Ezuka & Ishida (1999) found the characteristic temperature of the underlying hard continuum to be typically  $kT \sim 20$  keV. Although with a large source-to-source scatter, the average EW of the 6.4-, 6.7- and 6.9-keV lines across this CV sample were roughly  $\sim 100$ ,  $\sim 170$  and  $\sim 100$  eV, respectively. Similar average EWs were reported in the parallel study by Hellier, Mukai & Osborne (1998). More recently, Hellier & Mukai (2004) investigated the X-ray spectra of five magnetic CVs observed at high spectral resolution with the *Chandra* High-energy Transmission Grating (HETG). Within this limited sample the average EWs were  $\sim 120$ ,  $\sim 160$  and  $\sim 110$  eV for the 6.4-, 6.7- and 6.9-keV lines, respectively. Finally, Bernardini et al. (2012) report the detection of intense Fe K $\alpha$  line emission in the X-ray spectra of nine recently identified IPs and quote the EW of the 6.4-keV fluorescent line, in all cases, to be in the range 130–220 eV.

In our earlier analysis (Section 4), we found that the emission spectra of the three hardest subgroups could be represented as a hard continuum plus Fe lines. We modelled the hard continuum as a power law of photon index  $\Gamma = 1.55$  but obtained equivalent results when the power law was replaced by a thermal bremsstrahlung continuum with  $kT \approx 20$  keV. The average EW of the He-like Fe line at 6.7 keV was  $170_{-32}^{+35}$  eV. Similarly, the EWs of the 6.4- and 6.9-keV Fe lines were  $89_{-25}^{+26}$  and  $81_{-29}^{+30}$  eV, respectively, i.e. roughly half that of the 6.7-keV line. Evidently, these spectral characteristics are fully consistent with those of known magnetic CVs.

The inference is that a sizeable fraction of our current hard-band sample may be magnetic CVs, albeit with counterparts which are in general too faint to pick out reliably from available NIR catalogues.

However, it is necessary to consider what impact non-CV interlopers might have on the measurements deriving from the stacked (i.e. sample-averaged) spectra. For example, we noted in Section 5 that, based on source count estimates, AGN might contribute up to 50 per cent of the hardest subgroup of sources. Compton-thin AGN are characterized by power-law continuum spectra with  $\Gamma \approx 1.7$  plus a prominent Fe fluorescence line with an EW typically in the range 20–120 eV (see Fukazawa 2011; Chaudhary et al. 2012 and references therein). Clearly any dilution of the CV contribution by AGN would tend to reduce the EW of the 6.7- and 6.9-keV lines, whilst having relatively little impact on the 6.4-keV measurements. There is perhaps slight evidence for this from a comparison of the results from the three hardest subgroups (on the presumption that the high column density through the Galactic disc places AGN preferentially in the hardest subgroup); however, it seems unlikely that this has introduced a strong overall bias in our Fe line EW measurements.

Having demonstrated, on spectral grounds, that magnetic CVs very likely represent a significant Galactic population at the intermediate to faint X-ray fluxes encompassed by our *XMM-Newton* source sample, what are the implications for the origin of the GRXE? In a recent study of the distribution of K-shell line emission along the Galactic plane observed by *Suzaku*, Uchiyama et al. (2013) find that the average EWs of the 6.4-, 6.7- and 6.9-keV lines associated with the GRXE are  $\approx 110$ ,  $\approx 490$  and  $\approx 110$  eV (see also Ebisawa et al. 2008; Yamauchi et al. 2009). As noted by Uchiyama et al. (2013) and other authors, although the 6.4- and 6.9-keV line EWs measured for the GRXE match those of magnetic CVs, it appears that the EW of the 6.7-keV line is in a factor of 2–3 times higher than is typical of such systems.

Of course, our present measurements pertain to sources with X-ray fluxes down to a limiting threshold of roughly  $2 \times 10^{-13}$  erg cm<sup>-2</sup> s<sup>-1</sup> (2–10 keV), by which point less than  $\sim 10$  per cent of GRXE intensity has been resolved (Hands et al. 2004; Ebisawa et al. 2005). In fact it has been pointed out that in order to resolve 90 per cent of the GRXE, a sensitivity limit of  $\sim 10^{-16}$  erg cm<sup>-2</sup> s<sup>-1</sup> (2–10 keV) will be needed, encompassing sources with luminosities as low as  $10^{29-30}$  erg s<sup>-1</sup> at the Galactic Centre distance (Revnivtsev et al. 2006, 2009, 2011; Morihana et al. 2013).

At these much fainter fluxes and luminosities, the balance across the various X-ray emitting populations will very likely change (e.g. Morihana et al. 2013 – although for a counter argument see Ruitter, Belczynski & Harrison 2006; Hong et al. 2009; Hong 2012). For example, non-magnetic CVs, which comprise the majority of the local CV population, are well-established sources of X-ray emission at the lower end of the range of the luminosity exhibited by magnetic systems (Baskill, Wheatley & Osborne 2005; Rana et al. 2006; Byckling et al. 2010; Reis et al. 2013) and hence may make a substantial contribution. Conceivably Galactic scale influences such as the metallicity or binarity of the stellar population may also play a role. For example, a significant increase in the number density of extreme RSCVn binaries towards the inner galaxy (e.g. Revnivtsev et al. 2011), with spectra dominated by relatively hard ( $\sim 3$  keV) coronal plasma, could in principle provide the required 6.7-keV EW enhancement.

## 7 CONCLUSIONS

We have shown that the average spectral properties, particularly the Fe line properties, of hard X-ray sources discovered serendipitously at intermediate to faint fluxes in *XMM-Newton* observations of the

Galactic plane match those of known magnetic CVs. Unfortunately this X-ray source population is too faint to be readily identified via the cross-correlation of the *XMM-Newton* positions with current NIR source catalogues. However, our analysis does provide an indication that, in Galactic X-ray surveys extending down to a modest  $10^{-13}$  erg cm $^{-2}$  s $^{-1}$  (2–10 keV), an appropriate combination of sub-arcsec X-ray astrometry and deep high-resolution NIR imaging will reveal substantial numbers of (relatively high  $L_X$ ) CVs.

Although, the stacked spectra of the hard *XMM-Newton* sources show a fair resemblance to the integrated spectrum of the GRXE, there are some differences in detail, notably a factor of 2–3 discrepancy in the observed EW of the 6.7-keV He-like Fe line. This discrepancy presumably stems from the changing makeup of the X-ray source population at a flux threshold some three orders of magnitude fainter than probed by the *XMM-Newton* observations.

## ACKNOWLEDGEMENTS

This publication makes use of data products from 2MASS, which is a joint project of the University of Massachusetts and the Infrared Processing and Analysis Center/California Institute of Technology, funded by the National Aeronautics and Space Administration and the National Science Foundation. In carrying out this research, use has been made of ALADIN, VizieR and SIMBAD at the CDS, Strasbourg, France. The X-ray data sets were obtained from the *XMM-Newton* Science Archive (XSA).<sup>6</sup>

## REFERENCES

Agrawal P. C., Riegler G. R., White N. E., 1981, *MNRAS*, 196, 73  
 Ak T., Bilir S., Ak S., Retter A., 2007, *New Astron.*, 12, 446  
 Ak T., Bilir S., Ak S., Eker Z., 2008, *New Astron.*, 13, 133  
 Anders E., Grevesse N., 1989, *Geochim. Cosmochim. Acta*, 53, 197  
 Anderson G. E. et al., 2011, *ApJ*, 727, 105  
 Arnaud K., 1996, in Jacoby G. H., Barnes J., eds, *ASP Conf. Ser. Vol. 101, Astronomical Data Analysis Software and Systems V*. Astron. Soc. Pac., San Francisco, p. 17  
 Baskill D. S., Wheatley P. J., Osborne J. P., 2005, *MNRAS*, 357, 626  
 Bernardini F., de Martino D., Falanga M., Mukai K., Matt G., Bonnet-Bidaud J.-M., Masetti N., Mouchet M., 2012, *A&A*, 542, A22  
 Byckling K., Mukai K., Thorstensen J. R., Osborne J. P., 2010, *MNRAS*, 408, 2298  
 Capelli R., Warwick R. S., Porquet D., Gillessen S., Predehl P., 2012, *A&A*, 545, A35  
 Chaudhary P., Brusa M., Hasinger G., Merloni A., Comastri A., Nandra K., 2012, *A&A*, 537, A6  
 Covey K. R. et al., 2007, *AJ*, 134, 2398  
 Cropper M., Ramsay G., Wu K., 1998, *MNRAS*, 293, 222  
 Cropper M., Wu K., Ramsay G., Kocabiyyik A., 1999, *MNRAS*, 306, 684  
 Cutri R. M. et al., 2003, *The IRSA 2MASS All-Sky Point Source Catalog*, NASA/IPAC Infrared Science Archive. IPAC/Caltech, Pasadena, available at: <http://irsa.ipac.caltech.edu/applications/Gator/>  
 Ebisawa K., Bourban G., Bodaghee A., Mowlave N., Courvoisier T. J.-L., 2003, *A&A*, 411, 59  
 Ebisawa K. et al., 2005, *ApJ*, 635, 214  
 Ebisawa K. et al., 2008, *PASJ*, 60, S223  
 Ezuka H., Ishida M., 1999, *ApJS*, 120, 277  
 Fukazawa Y. et al., 2011, *ApJ*, 727, 19  
 Grimm H.-J., Gilfanov M., Sunyaev R., 2002, *A&A*, 391, 923  
 Güdel M., 2004, *A&AR*, 12, 71

Hands A. D. P., Warwick R. S., Watson M. G., Helfand D. J., 2004, *MNRAS*, 351, 31  
 Heard V., Warwick R. S., 2013, *MNRAS*, 428, 3462  
 Hellier C., Mukai K., 2004, *MNRAS*, 352, 1037  
 Hellier C., Mukai K., Osborne J. P., 1998, *MNRAS*, 297, 526  
 Hertz P., Grindlay J. E., 1984, *ApJ*, 278, 137  
 Hong J., 2012, *MNRAS*, 427, 1633  
 Hong J., Schegel E. M., Grindlay J. E., 2004, *ApJ*, 614, 508  
 Hong J., van den Berg M., Grindlay J. E., Laycock S., 2009, *ApJ*, 706, 223  
 Kaneda H., Makishima K., Yamauchi S., Koyama K., Matsuzaki K., Yamasaki N. Y., 1997, *ApJ*, 491, 638  
 Koyama K., Makishima K., Tanaka Y., Tsunemi H., 1986a, *PASJ*, 38, 121  
 Koyama K., Ikeuchi S., Tomisaka K., 1986b, *PASJ*, 38, 503  
 Koyama K., Maeda Y., Sonobe T., Takeshima T., Tanaka Y., Yamauchi S., 1996, *PASJ*, 48, 249  
 Koyama K. et al., 2007, *PASJ*, 59, 245  
 Krivonos R., Revnivtsev M., Churazov E., Sazonov S., Grebenev S., Sunyaev R., 2007, *A&A*, 463, 957  
 Lawrence A. et al., 2007, *MNRAS*, 379, 1599  
 Laycock S., Grindlay J., van den Berg M., Zhao P., Hong J., Koenig X., Schlegel E. M., Persson S. E., 2005, *ApJ*, 634, L53  
 Liu Q. Z., van Paradijs J., van den Heuvel E. P. J., 2007, *A&A*, 469, 807  
 Mauerhan J. C., Muno M. P., Morris M. R., Bauer F. E., Nishiyama S., Nagata T., 2009, *ApJ*, 703, 30  
 Mauerhan J. C., Muno M. P., Morris M. R., Stolovy S. R., Cotera A., 2010, *ApJ*, 710, 706  
 Morihana K., Tsujimoto M., Yoshida T., Ebisawa K., 2013, *ApJ*, 766, 14  
 Motch C. et al., 2010, *A&A*, 523, A92  
 Muno M. P. et al., 2004, *ApJ*, 613, 1179  
 Nebot Gómez-Morán A. et al., 2013, *A&A*, 553, A12  
 Nishiyama S. et al., 2013, *ApJ*, 769, L28  
 Nobukawa M., Koyama K., Matsumoto H., Tsuru T. G., 2009, *PASJ*, 61, 93  
 Rana V. R., Singh K. P., Schegel E. M., Barrett P. E., 2006, *ApJ*, 642, 1042  
 Reis R. C., Wheatley P. J., Gänsicke B. T., Osborne J. P., 2013, *MNRAS*, 430, 1994  
 Revnivtsev M., Sazonov S., Gilfanov M., Churazov E., Sunyaev R., 2006, *A&A*, 452, 169  
 Revnivtsev M., Sazonov S., Krivonos R., Ritter H., Sunyaev R., 2008, *A&A*, 489, 1121  
 Revnivtsev M., Sazonov S., Churazov E., Forman W., Vikhlinin A., Sunyaev R., 2009, *Nature*, 458, 1142  
 Revnivtsev M., Sazonov S., Forman W., Churazov E., Sunyaev R., 2011, *MNRAS*, 414, 495  
 Ritter H., Kolb U., 2003, *A&A*, 404, 301  
 Ruiter A. J., Belczynski K., Harrison T. E., 2006, *ApJ*, 640, L167  
 Sazonov S., Revnivtsev M., Gilfanov M., Churazov E., Sunyaev R., 2006, *A&A*, 450, 117  
 Sidoli L., Merghetti S., Favata F., Oosterbroek T., Parmar A. N., 2006, *A&A*, 456, 287  
 Skrutskie M. F. et al., 2006, *AJ*, 131, 1163  
 Strickland D. K., Heckman T. M., Weaver K. A., Dahlem M., 2000, *AJ*, 120, 2965  
 Strong A. W., Diehl R., Halloin H., Schnfelder V., Bouchet L., Mandrou P., Lebrun F., Terrier R., 2005, *A&A*, 444, 495  
 Sugizaki M., Mitsuda K., Kaneda H., Matsuzaki K., Yamauchi S., Koyama K., 2001, *ApJS*, 134, 77  
 Tanaka Y., 2002, *A&A*, 382, 1052  
 Tanaka Y., Yamauchi S., 2010, in Makishima K., ed., *Proc. 3rd Suzaku Conf., The Energetic Cosmos: From Suzaku to ASTRO-H*, JAXA-SP-09-008E. Japan Aerospace Exploration Agency (JAXA), Tokyo  
 Uchiyama H., Nobukawa M., Tsuru T. G., Koyama K., Matsumoto H., 2011, *PASJ*, 63, 903  
 Uchiyama H., Nobukawa M., Tsuru T. G., Koyama K., 2013, *PASJ*, 65, 19

<sup>6</sup> <http://xmm.esac.esa.int/xsa/>

Valinia A., Marshall F. E., 1998, *ApJ*, 505, 134  
 Valinia A., Tatischeff V., Arnaud K., Ebisawa K., Ramaty R., 2000, *ApJ*, 543, 733  
 van den Berg M., Hong J., Grindlay J. E., 2009, *ApJ*, 700, 1702  
 van den Berg M., Penner K., Hong J., Grindlay J. E., Zhao P., Laycock S., Servillat M., 2012, *ApJ*, 748, 31  
 Warwick R. S., Turner M. J. L., Watson M. G., Willingale R., 1985, *Nature*, 317, 218  
 Warwick R. S., Pérez-Ramírez D., Byckling K., 2011, *MNRAS*, 413, 595 (Paper I)  
 Watson M. G. et al., 2009, *A&A*, 493, 339  
 Worrall D. M., Marshall F. E., Boldt E. A., Swank J. H., 1982, *ApJ*, 255, 111  
 Yamasaki N. Y. et al., 1997, *ApJ*, 481, 821  
 Yamauchi S., Koyama K., 1993, *ApJ*, 404, 620  
 Yamauchi S., Kaneda H., Koyama K., Makishima K., Matsuzaki K., Sonobe T., Tanaka Y., Yamasaki N., 1996, *PASJ*, 48, L15  
 Yamauchi S., Ebisawa K., Tanaka Y., Koyama K., Matsumoto H., Yamasaki N. Y., Takahashi H., Ezoe Y., 2009, *PASJ*, 61, S225  
 Yuasa T., Nakazawa K., Makishima K., Saitou K., Ishida M., Ebisawa K., Mori H., Yamada S., 2010, *A&A*, 520, A25  
 Yuasa T., Makishima K., Nakazawa K., 2012, *ApJ*, 753, 129

## APPENDIX A: THE 138 SERENDIPITOUS 2XMM SOURCES

**Table A1.** The source sample. The columns provide the following information (from left to right): the source and observation identification (ObsID) numbers, the IAU name, the pn net counts in the source spectrum and the broad-band HR.

Source	ObsID	IAU name 2XMM	pn net counts	HR
210866	0400910201	J145847.6–581623	369	–0.89
211566	0405390401	J153615.4–575415	834	–0.78
142052	0203910101	J154951.7–541630	709	–0.04
142126	0203910101	J155037.5–540722	123	–0.22
212112	0406650101	J161414.2–514857	270	–0.70
212156	0406650101	J161437.3–512935	593	–0.91
212182	0406650101	J161448.5–514830	802	–0.93
212210	0406650101	J161502.8–513802	362	–0.80
212279	0406650101	J161552.6–513756	884	0.01
212289	0406650101	J161601.7–513715	205	–0.40
212343	0406750201	J162048.8–494214	250	–0.19
212403	0403280201	J162608.1–490010	183	–0.65
148350	0307170201	J163737.0–472951	215	–0.95
148374	0307170201	J163748.3–472220	388	0.13
148388	0307170201	J163756.4–471949	515	–0.88
148402	0307170201	J163802.7–471357	239	0.98
148411	0307170201	J163808.5–472607	223	0.87
148493	0307170201	J163835.9–472145	441	0.92
148497	0303100101	J163837.7–464725	118	0.94
148502	0303100101	J163839.2–470618	129	0.05
148509	0307170201	J163840.9–471952	169	–0.62
148513	0307170201	J163842.3–473008	257	0.95
148559	0303100101	J163855.1–470146	470	–0.04
148620	0303100101	J163914.5–470020	345	–0.81
148624	0307170201	J163915.1–472310	253	–0.89
148707	0307170201	J163937.8–471951	118	1.00
148790	0303100101	J164004.1–470419	283	–0.88
150181	0112460201	J165340.2–395709	139	0.40
150188	0112460201	J165341.1–395735	122	0.19
150845	0112460201	J165443.1–394804	172	–0.20
150957	0112460201	J165515.6–394544	224	–0.60
151081	0200900101	J165739.8–425715	437	0.95

**Table A1** – *continued*

Source	ObsID	IAU name 2XMM	pn net counts	HR
151278	0200900101	J165906.6–424210	275	0.07
213203	0406752301	J170019.2–422019	392	1.00
213412	0406750301	J170451.7–410949	178	0.41
152200	0144080101	J170713.1–405414	208	–0.70
152262	0144080101	J170819.6–404606	124	0.94
214415	0401960101	J171808.7–382604	375	–0.82
214420	0401960101	J171813.6–382516	355	0.16
214437	0401960101	J171830.9–382704	225	–0.79
214440	0401960101	J171833.0–382749	246	–0.92
154343	0112201401	J172945.2–335028	152	0.26
155792	0112971901	J174351.2–284638	178	–0.58
155865	0112970701	J174423.3–291743	569	0.03
215274	0406580201	J174434.4–301521	317	–0.95
215297	0406580201	J174441.2–301647	215	–0.90
156010	0112970701	J174458.2–292507	176	0.96
156080	0103261301	J174508.0–303906	110	0.98
215498	0400340101	J174541.1–300055	251	0.23
215524	0400340101	J174558.0–295738	129	0.98
157004	0112970201	J174645.2–281547	212	1.00
157045	0112970201	J174654.6–281658	146	–0.19
157148	0205240101	J174716.1–281047	441	0.96
157193	0205240101	J174722.8–280905	363	0.99
157247	0205240101	J174730.8–281347	110	–0.82
157393	0205240101	J174804.1–281446	104	0.92
157432	0205240101	J174814.0–281621	62	1.00
157439	0205240101	J174816.9–280750	225	0.99
157544	0112970101	J174848.0–281240	402	0.37
157571	0112970101	J174858.3–281422	172	0.23
158008	0206990101	J175035.2–311825	197	–0.48
158050	0206990101	J175046.8–311629	237	–0.02
158316	0307110101	J175136.4–295016	170	–0.77
158318	0307110101	J175137.1–295522	300	0.39
158373	0307110101	J175155.9–295113	514	–0.38
158409	0307110101	J175233.1–293944	203	–0.57
158631	0302570101	J175446.3–285659	202	0.46
158719	0206590201	J175516.6–293655	243	0.11
158755	0302570101	J175528.8–290002	491	0.60
158765	0302570101	J175533.4–290148	272	–0.81
158770	0302570101	J175534.1–291136	394	0.75
158784	0302570101	J175539.0–285637	390	–0.88
158786	0302570101	J175540.7–290641	232	0.12
158847	0302570101	J175607.6–290752	220	0.56
158874	0302570101	J175624.0–290924	249	–0.60
158926	0099760201	J175656.5–214833	134	–0.70
158936	0099760201	J175659.8–214350	806	–0.04
158945	0099760201	J175701.8–213336	226	0.03
159002	0099760201	J175722.3–213729	231	0.49
159099	0099760201	J175741.1–214309	580	–0.98
159225	0099760201	J175800.6–213856	538	0.37
160502	0135742801	J180154.4–224647	258	–0.97
162701	0024940201	J180706.8–192559	296	–0.94
162842	0024940201	J180736.4–192658	338	0.06
162991	0024940201	J180802.0–191505	325	–0.68
163006	0024940201	J180804.4–192453	311	–0.04
163107	0024940201	J180822.4–191813	202	–0.65
163452	0301270401	J180929.5–194126	310	–0.81
163464	0301270401	J180932.7–194654	209	–0.85
163510	0301270401	J180942.9–194544	288	1.00
163664	0301270401	J181009.8–194829	357	–0.21
163722	0152835701	J181024.8–183712	216	0.79
165111	0152834901	J181848.0–152753	397	–0.91
165128	0152834501	J181851.2–155920	352	0.85
165294	0152834501	J181913.4–160118	320	0.45

Table A1 – continued

Source	ObsID	IAU name 2XMM	pn net counts	HR
165845	0040140201	J182258.0–135322	185	0.94
165849	0040140201	J182304.3–135036	154	0.90
165864	0040140201	J182319.7–134009	275	0.78
165865	0040140201	J182321.2–134643	316	–0.75
165873	0040140201	J182342.7–134947	510	–0.58
165933	0051940101	J182524.5–114525	293	0.67
165958	0104460701	J182533.6–121452	189	–0.89
166079	0051940301	J182626.7–112854	203	0.79
166111	0135745401	J182639.6–114216	202	–0.75
166331	0104460401	J182756.7–110448	174	0.90
166437	0051940401	J182830.8–114514	265	–0.83
166459	0104460401	J182845.5–111710	557	–0.81
166461	0135745701	J182847.6–101337	551	–0.98
166477	0135745701	J182855.9–095414	321	0.88
166494	0104460901	J182905.6–104635	178	0.84
166583	0135745801	J182948.6–110604	240	0.46
166713	0135746301	J183038.2–100246	223	0.80
166900	0135741601	J183251.4–100106	102	0.22
217348	0400910101	J183345.2–081828	593	–0.95
167248	0302560301	J183514.6–083740	168	–0.04
217485	0400910301	J183711.5–063315	212	–0.96
167514	0301880901	J183939.8–024935	185	–0.27
167528	0301880901	J183947.4–024504	216	–0.81

Table A1 – continued

Source	ObsID	IAU name 2XMM	pn net counts	HR
217584	0302970301	J184226.1–035947	403	0.99
217586	0302970301	J184226.9–035536	181	–0.47
168031	0046540201	J184441.9–030551	466	0.48
168039	0017740601	J184447.7+011131	316	–0.86
168124	0203850101	J184720.6–015248	227	0.98
168158	0207010201	J184747.3–011910	149	0.95
217784	0302970801	J184805.8–022821	231	–0.03
217813	0302970801	J184816.8–022524	436	0.97
217816	0406140201	J184817.4–031907	675	0.89
168249	0136030101	J184953.6–003007	355	–0.60
168254	0136030101	J184958.7–002018	170	0.58
168272	0136030101	J185020.0–001313	449	–0.83
168311	0017740401	J185125.1+000742	182	–0.94
168323	0017740401	J185139.1+001635	378	–0.09
168324	0017740401	J185139.9+001308	191	–0.95
168428	0017740401	J185233.2+000638	189	–0.14
169142	0136030201	J190109.0+045751	303	0.61
169450	0305580201	J190704.0+092532	172	0.56
169482	0305580101	J190717.7+092421	288	0.42
169532	0305580101	J190742.0+090713	270	0.83

This paper has been typeset from a  $\text{\TeX}/\text{\LaTeX}$  file prepared by the author.